



Contents lists available at ScienceDirect

International Journal of Mining Science and Technology

journal homepage: [www.elsevier.com/locate/ijmst](http://www.elsevier.com/locate/ijmst)

## Experimental and numerical studies on progressive debonding of grouted rock bolts



Hao Shi<sup>a,b</sup>, Lei Song<sup>a,\*</sup>, Houquan Zhang<sup>a</sup>, Wenlong Chen<sup>c</sup>, Huasheng Lin<sup>d</sup>, Danqi Li<sup>e</sup>, Guozhu Wang<sup>a</sup>, Huayun Zhao<sup>a</sup>

<sup>a</sup> State Key Laboratory for Geomechanics & Deep Underground Engineering, School of Mechanics & Civil Engineering, China University of Mining and Technology, Xuzhou 221116, China

<sup>b</sup> School of Civil Engineering and Architecture, Anhui University of Science and Technology, Huainan 232001, China

<sup>c</sup> School of Water, Energy and Environment, Cranfield University, Cranfield MK43 0AL, UK

<sup>d</sup> Glencore Coal Assets Australia, Mount Thorley, NSW 2330, Australia

<sup>e</sup> WA School of Mines: Minerals, Energy and Chemical Engineering, Curtin University, Kalgoorlie WA6430, Australia

### ARTICLE INFO

#### Article history:

Received 7 June 2020

Received in revised form 6 July 2021

Accepted 7 October 2021

Available online 18 October 2021

#### Keywords:

Bolt pull-out test  
Bolt failure process  
AE positioning  
Meso-interaction  
PFC<sup>2D</sup> simulation

### ABSTRACT

Understanding the mechanism of progressive debonding of bolts is of great significance for underground safety. In this paper, both laboratory experiment and numerical simulation of the pull-out tests were performed. The experimental pull-out test specimens were prepared using cement mortar material, and a relationship between the pull-out strength of the bolt and the uniaxial compressive strength (UCS) of cement mortar material specimen was established. The locations of crack developed in the pull-out process were identified using the acoustic emission (AE) technique. The pull-out test was reproduced using 2D Particle Flow Code (PFC<sup>2D</sup>) with calibrated parameters. The experimental results show that the axial displacement of the cement mortar material at the peak load during the test was approximately 5 mm for cement-based grout of all strength. In contrast, the peak load of the bolt increased with the UCS of the confining medium. Under peak load, cracks propagated to less than one half of the anchorage length, indicating a lag between crack propagation and axial bolt load transmission. The simulation results show that the dilatation between the bolt and the rock induced cracks and extended the force field along the anchorage direction; and, it was identified as the major contributing factor for the pull-out failure of rock bolt.

© 2021 Published by Elsevier B.V. on behalf of China University of Mining & Technology. This is an open access article under the CC BY-NC-ND license (<http://creativecommons.org/licenses/by-nc-nd/4.0/>).

### 1. Introduction

For slope, mining, tunnel and other geological engineering, timely support is required since the start of the excavation, as it is crucial to ensure long-term stability [1–3]. At present, rock bolt is commonly used in supporting system for it is simple in operation and cheap in cost [4]. The bolt support, however, fails under long duration of external loads or among fragile geological conditions. The mechanism underneath the failure of bolt support is not clear, which poses dangers to the project and personnel [5,6]. Therefore, it is pivotal to study the physics, i.e., the bolt-rock interaction, during the failure process of the bolt support.

The mechanical properties of bolt support have been extensively studied. Experimental researches on this topic can be roughly summarized into three groups based on their research objects. The first group focuses on the stress distribution along

the bolt, obtaining the function distribution of the shear stress and deriving the corresponding calculation theories or models [7–11]. The second group studies the effect of bolt size or grout property on anchorage strength, i.e., by investigating the bolt diameter, length [12,13] as well as the grout length, diameter and strength [14–16]. The third group mainly studies the anchoring effect of bolt. The bolt support effects were investigated by changing bolt preload [17,18], loading rate [19,20], confining pressure [21] and support density [22,23]. The above research is of great significance for understanding the supporting effect of bolt, but is limited on bolt under normal supporting state, which makes it difficult to reveal the meso-mechanism of bolt support failure. Therefore, it is necessary to study the progressive debonding process of bolt. Due to the fact that the bolt is the hidden member deep into the rock mass [24], the debonding failure process of the bolt is very difficult to capture directly by experimental methods [25]. Some researchers noticed this problem and turned to solve it with numerical simulation [26–30]. The finite element method was widely used for this specific problem [31–33], but

\* Corresponding author.

E-mail address: [songlei\\_cumt@163.com](mailto:songlei_cumt@163.com) (L. Song).

with an over-simplified bolt-rock interface. In particular, the physical existence of bolt ribs was often ignored [31,33], and the mechanical action of the bolt-rock interface was simply characterized by assigned parameters, which fails in fully revealing the mechanism of bolt-rock interaction. Moreover, bolt support is greatly affected by the properties of rock mass [34], but the current research on bolt-rock interaction rarely accounts for the influence of rock mass properties (such as strength). The goal of this research is to reveal the bolt-rock meso-interaction considering the physical existence of bolt ribs and the influence of rock strength.

To this end, both indoor experiment and numerical simulation were performed. Cement mortar material with good homogeneity was used to pour the bolt pull-out specimens to be used in the experiment. The corresponding relationship between the bolt pull-out strength and the Uniaxial Compressive Strength (UCS) of cement mortar material specimen is established based on test results. Next, a pull-out model using the two dimensional Particle Flow Code (PFC<sup>2D</sup>) was set-up with parameters calibrated using the experimental results. Both experimental and simulated bolt pull-out failure processes were analyzed to reveal the bolt-rock meso-interaction during the bolt pull-out failure process.

## 2. Pull-out experiment of rock bolt

### 2.1. Selection of parameters

Preliminary experiments were carried out to test the feasibility of the proposed method. Parameters including the dimension of the test samples, the grout quality, anchorage length, displacement rate and number of test samples were finalized.

The cement-based samples were chosen considering the homogeneity characteristics of such material. Under normal circumstances, the strength of cement mortar specimens will increase to about 80% of the standard strength after 12 days curing. To introduce variation in the strength, the bolt pull specimens of different curing time were prepared, i.e., with 1, 3, 5, 7 and 12 days curing. In addition, appropriate aggregate ratios of the test samples should be chosen to easily distinguish the axial load carrying capacity under different testing conditions with varying curing time. After many trials, the M25 cement mortar was finally adopted, and the corresponding ratio between 425 cement: medium sand: water is 1:4.03:0.75. Anchorage length of 25 cm for the grouted rock bolt was chosen to ensure the stability of the rock bolt during the full displacement of the rock bolt. To mitigate the size effect, preliminary tests on samples with various dimensions were conducted to determine the minimum thickness of the confining medium, which is 35 cm. The confining medium was casted to a dimension of 30 cm in height and 40 cm in length and width. A 0.005 mm/s displacement rate was set to provide a static loading environment. In total, 10 test samples were casted under 5 different grout curing time, each with 2 replication tests.

### 2.2. Test sample preparation

The test samples with parameters determined in the preliminary tests were casted, as shown in Fig. 1. The rock bolt was placed in the center of the test sample. The materials for casting samples were carefully mixed. Finally, the casted test samples were polished and then kept in a high moisture condition for various curing time.

### 2.3. AE receiver installation

All cured samples were hoisted onto a platform for installation of AE receivers (see Fig. 2a). The DS5 AE receivers were attached onto the test samples using silicon glue, as shown in Fig. 2b and c.



Fig. 1. Pouring and curing of pulling specimens.

The locations of eight AE receivers are illustrated in Fig. 3. Although the  $x$  and  $z$  coordinates of the center point of the AE receivers in Fig. 3 cannot cover the entire model (the  $x$  coordinate is 0.5 or 29.5 cm, and the  $z$  coordinate is  $-19.5$  or 19.5 cm), it does not prevent the measurement of the AE sources inside the entire specimen.

### 2.4. Pull-out test

The pull-out test facility included a loading frame, a console, and an AE detection equipment (see Fig. 4a). The loading end of the rock bolt was fixed with the anchor lock (see Fig. 4b). A constant displacement rate of 0.005 mm/s was utilized in the loading process. The rock bolt was pulled up to 20 mm displacement leading to approximately one hour total test duration. The AE sampling frequency was set to 5 MHz, and the trigger gate value was 100 mV for all eight channels.

## 3. Experimental results and analysis

### 3.1. Load-displacement curves of the specimens under different curing times

The load-displacement curves of the pull-out tests of test samples with different curing periods are shown in Fig. 5. It can be seen



Fig. 2. Hoisting of test specimens as well as fixed points and the adhesive installation of the AE receivers.

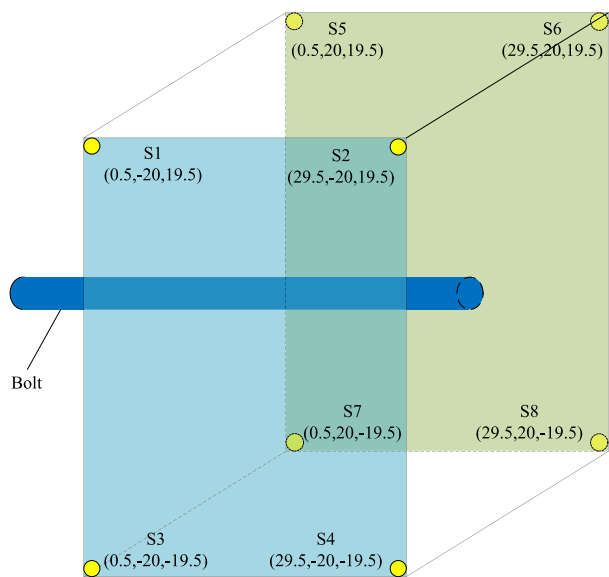


Fig. 3. Schematic diagram of the AE receiver locations.

that the replicated test results are consistent with one another. Both the peak load carrying capacity and the initial stiffness (i.e., the slope of the load–displacement curve before the peak) increase with the curing time. In contrast, the axial displacement at the peak load carrying capacity is approximately 5 mm, which is half of the rib space of the rock bolt, regardless of curing time. Interestingly, a second peak above the axial load emerges during the residual level only for samples cured for less than 5 days. This discrepancy in the observations might be associated with the combined effect of the axial bolt load and the shear action between the bolt rib and the surrounding cement mortar.

The fluctuation in the axial loading may be attributed to the 10 mm space in between ribs in the rock bolt. It can be also seen that the second peak above the axial load always occurred after 10 mm axial displacement, as shown in Fig. 5. A highly likely explanation is that a 10 mm rib space leads to approximately 10 mm cyclic displacement. In other words, for every successive 10 mm axial displacement, the axial load of the rock bolt increases to

the peak values and is followed by a reduction (see Fig. 5a-c). However, such behavior of the rock bolt is less phenomenal for stronger test samples with longer curing time (see Fig. 5d-e).

Therefore, the curing time of the test sample has a significant influence on the performance of the rock bolt under axial loading. The selection of representative test samples for the numerical simulations followed this guidance.

### 3.2. Influence of test sample strength

The influence of the test sample strength on the performance of the rock bolt under axial loading was investigated in this section. The material used for the test samples were casted according to the International Society for Rock Mechanics (ISRM) standard for UCS test using the mould shown in Fig. 6 which has a diameter of 50 mm and length of 100 mm. The cylindrical samples were cured with various time frame ranging from 1 day to 12 days in consistent with the pull-out tests. The prepared samples were tested following the ISRM UCS testing procedures (see Fig. 7).

The relationship between the bearing capacity of the bolt and the UCS of the test sample is present in Fig. 8. It can be seen that the peak load carrying capacity of the bolt increases approximately linearly with the UCS of the test sample indicating that the strength of the rockmass in the field will have a significant effect on the support capacity of the rock bolt. As such, for weaker underground rockmass, more rock bolts or more competent alternative ground support approaches should be implemented.

### 3.3. AE crack positioning

#### 3.3.1. AE time-difference positioning algorithm (Geiger algorithm based on the least square method)

P wave has fast propagation speed and the identification of its first arrival time is easy. Owing to these properties, P wave is widely used in AE crack positioning. The current often used AE crack positioning methods include the simplex algorithm, the least square method (LSM) and the Geiger algorithm. Among these methods, the Geiger algorithm [37–39] based on the LSM has better positioning effect and was used in this paper. The position identifying process using this algorithm can be described as: (1) approximating the initial solution of the algorithm; (2) using the LSM to calculate the correction value; (3) adding the correction

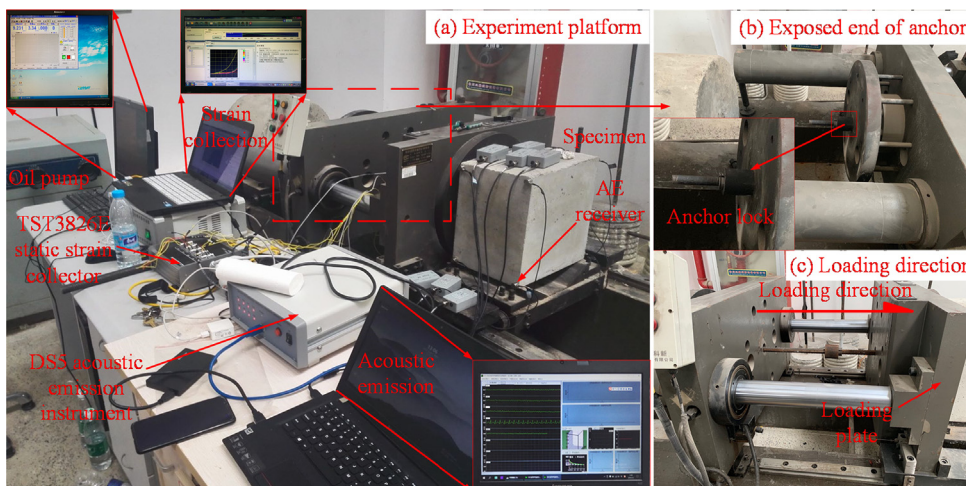


Fig. 4. System for bolt pull-out experiment.



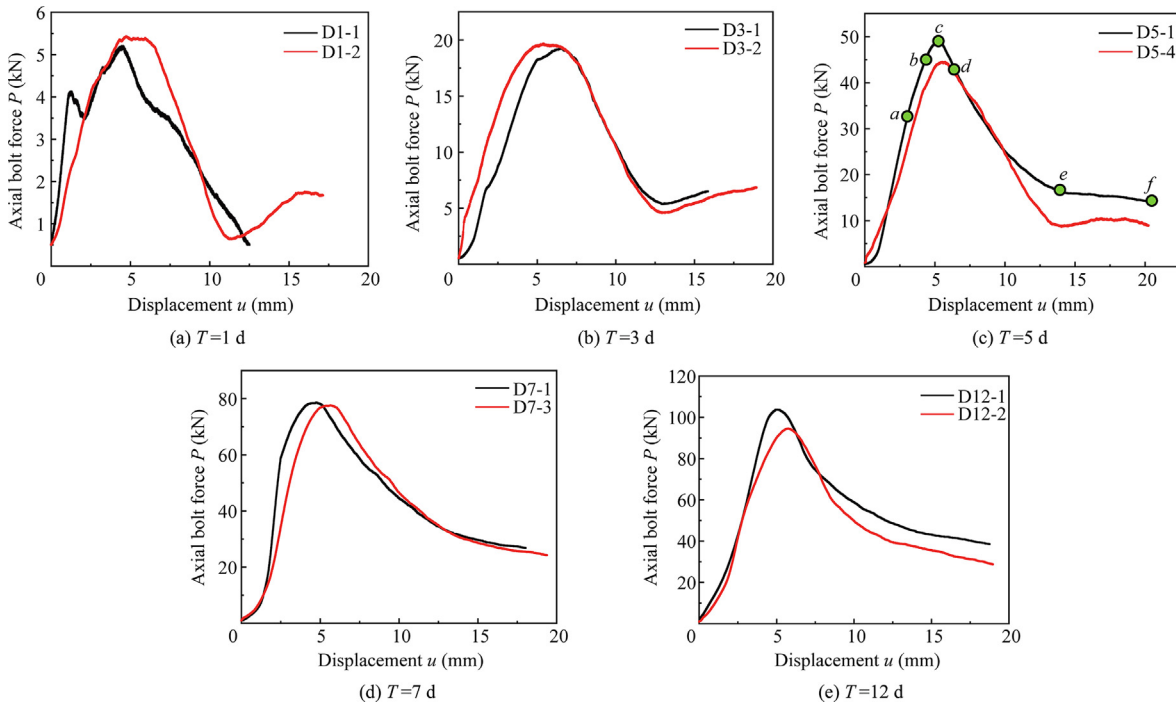


Fig. 5. The load–displacement curves of the pull-out specimens.

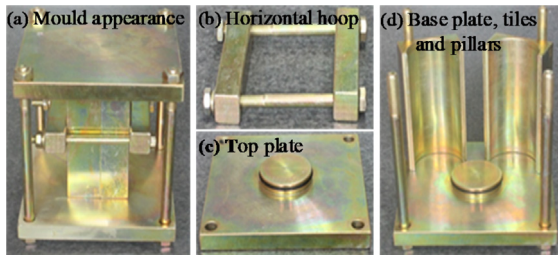


Fig. 6. Standard specimen mould and its composition [35–37].

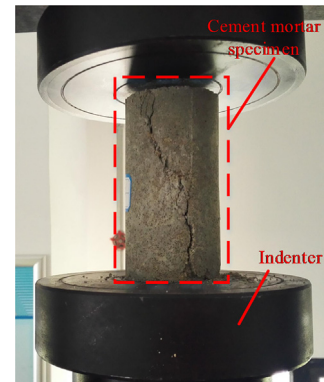


Fig. 7. Uniaxial compression test of standard specimen.

value to the initial solution to form a new optimal solution; (4) bringing the optimal solution into the objective function and calculating the error. This process should be repeated until the error is less than a defined accuracy. A global optimal solution is obtained at the end of the iteration. The objective function ( $f_{\min}$ , also called the time error function) is as following,

$$f_{\min} = \sum_{i=1}^n \left( \left[ (x - x_i)^2 + (y - y_i)^2 + (z - z_i)^2 \right]^{1/2} / v_p - (t_i - t_0) \right)^2 \quad (1)$$

where  $n$  is the number of AE receivers;  $(x, y, z)$  and  $(x_i, y_i, z_i)$  represent the coordinates of the AE source and the  $i$ -th AE receiver, respectively;  $v_p = 2910$  m/s denotes the velocity of P wave and is determined by lead-break test;  $t_0$  and  $t_i$  represent the time when the AE occurred and the time when the P wave propagated to the position of the  $i$ -th AE receiver, respectively.

The schematic diagram of the AE positioning is shown in Fig. 9. The positional relationship between the  $i$ -th receiver and the AE source can be expressed by the following formula:

$$\begin{aligned} & \left[ (x - x_i)^2 + (y - y_i)^2 + (z - z_i)^2 \right]^{1/2} \\ & = v_p(t_i - t_0), (i = 1, 2, \dots, n) \end{aligned} \quad (2)$$

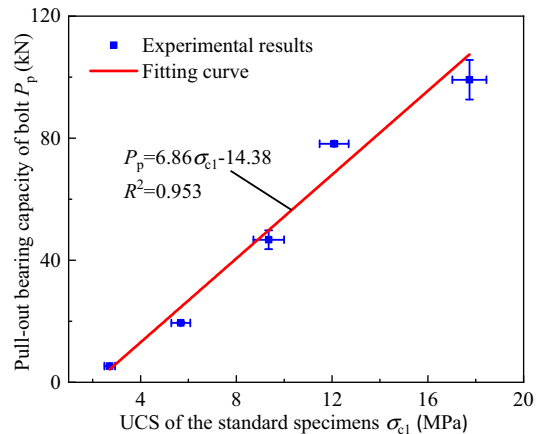


Fig. 8. Relation between peak load of bolt and UCS of standard specimens.

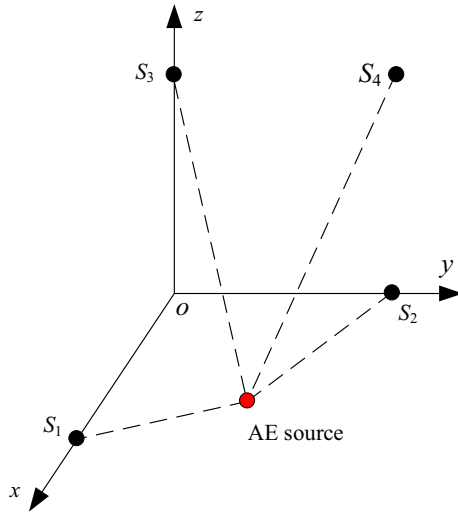


Fig. 9. Schematic diagram of AE crack positioning.

Taylor expansion of Eq. (2) leads to:

$$t_i = t_0 + t'_{0i} + \frac{\partial t'_i}{\partial x} \Delta x + \frac{\partial t'_i}{\partial y} \Delta y + \frac{\partial t'_i}{\partial z} \Delta z + \frac{1}{2!} \left( \frac{\partial^2 t'_i}{\partial x^2} \Delta x + \frac{\partial^2 t'_i}{\partial y^2} \Delta y + \frac{\partial^2 t'_i}{\partial z^2} \Delta z \right)^2 + \frac{1}{n!} \left( \frac{\partial^n t'_i}{\partial x^n} \Delta x + \frac{\partial^n t'_i}{\partial y^n} \Delta y + \frac{\partial^n t'_i}{\partial z^n} \Delta z \right)^2 \quad (3)$$

with  $t_{0i}$  being the elapsed time from the AE source to the  $i$ -th receiver. Within the allowable error range, the higher-order terms (second-order and over) of Eq. (2) can be safely neglected. As a result, Eq. (3) is simplified as:

$$t_i = t_0 + t'_{0i} + \frac{\partial t'_i}{\partial x} \Delta x + \frac{\partial t'_i}{\partial y} \Delta y + \frac{\partial t'_i}{\partial z} \Delta z \quad (4)$$

Set the auxiliary variable  $R$  to be:

$$R = \left[ (x - x_i)^2 + (y - y_i)^2 + (z - z_i)^2 \right]^{1/2} \quad (5)$$

According to Eqs. (4) and (5), the following formula can be obtained:

$$\begin{cases} \frac{\partial t'_i}{\partial x} = \frac{x_i - x}{v_p R} \\ \frac{\partial t'_i}{\partial y} = \frac{y_i - y}{v_p R} \\ \frac{\partial t'_i}{\partial z} = \frac{z_i - z}{v_p R} \end{cases} \quad (6)$$

$n$  receivers satisfying Eq. (4) leads to the following relation:

$$A \Delta \theta = B \quad (7)$$

where  $\Delta \theta$  is the correction value, and

$$A = \begin{bmatrix} 1 & \frac{\partial t'_1}{\partial x} & \frac{\partial t'_1}{\partial y} & \frac{\partial t'_1}{\partial z} \\ 1 & \frac{\partial t'_2}{\partial x} & \frac{\partial t'_2}{\partial y} & \frac{\partial t'_2}{\partial z} \\ \vdots & \vdots & \vdots & \vdots \\ 1 & \frac{\partial t'_n}{\partial x} & \frac{\partial t'_n}{\partial y} & \frac{\partial t'_n}{\partial z} \end{bmatrix}, \Delta \theta = \begin{bmatrix} \Delta t \\ \Delta x \\ \Delta y \\ \Delta z \end{bmatrix}, B = \begin{bmatrix} t_1 - t_0 \\ t_2 - t_0 \\ \vdots \\ t_n - t_0 \end{bmatrix}$$

Solving Eq. (7) using the LSM leads to:

$$\Delta \theta = (A^T A)^{-1} A^T B \quad (8)$$

The initial solution of the Geiger algorithm needs to be determined to start the iteration.

Firstly, the AE source should be located using LSM to ensure that the initial solution of the Geiger algorithm is within the convergence region [38,39].

Combining the number of receivers  $n$  and Eq. (2), the Eq. (9) can be established as following:

$$\left[ (x - x_i)^2 + (y - y_i)^2 + (z - z_i)^2 \right]^{1/2} = v_p (t_i - t_0), \quad (i = 1, 2, \dots, n) \quad (9)$$

Setting one of the equations as the elimination term and subtracting the elimination terms from the remaining terms, Eq. (9) can be simplified as:

$$m_i x + h_i y + l_i z + f_i t = g_i, \quad (i = 1, 2, \dots, n - 1) \quad (10)$$

The matrix form of Eq. (10) is as following:

$$CX = D \quad (11)$$

where,

$$C = \begin{bmatrix} m_1 & h_1 & l_1 & f_1 \\ m_2 & h_2 & l_2 & f_2 \\ \vdots & \vdots & \vdots & \vdots \\ m_{n-1} & h_{n-1} & l_{n-1} & f_{n-1} \end{bmatrix}, X = \begin{bmatrix} x \\ y \\ z \\ t \end{bmatrix}, D = \begin{bmatrix} g_1 \\ g_2 \\ \vdots \\ g_{n-1} \end{bmatrix}$$

Solving the Eq. (11) using the LSM gives the initial solution of the Geiger algorithm  $X$ , i.e.,

$$X = (C^T C)^{-1} C^T D \quad (12)$$

### 3.3.2. Results and analysis of AE crack positioning

The processing results of the positioning waveform signal show that when the curing time of the specimen is less than 5 days, the energy of acoustic emission signal generated by the debonding failure of the bolt is low due to the low strength of the specimen. Especially in the middle part of the specimen, the hydration reaction degree of the corresponding cement mortar is lower than that at the boundary of the specimen, leading to a bad positioning effect. The specimen D5-1 corresponding to the curing time of 5 days is selected for illustration.

**Screening of the AE location crack.** The AE signal was processed according to the positioning algorithm described in Section 3.3.1. Although the signal trigger threshold is set, there is inevitably a lot of noise in the positioning results. According to the introduction in Section 2.1, the anchoring length  $\times$  diameter of the bolt is 250 mm  $\times$  22 mm. Since the debonding process of the bolt body is only along the interface of the bolt, the crack distribution obtained by positioning detection should be in the cylindrical shape of length  $\times$  diameter = 250 mm  $\times$  22 mm under ideal circumstances. In order to eliminate noise interference as much as possible, only cracks distributed in the intervals of  $-4$  cm  $< y$  less than 4 cm,  $-4$  cm  $< z$  less than 4 cm and  $0$  cm  $< x$  less than 27 cm and trigger energy greater than 0.3 are retained. After the above screening treatment, the crack distribution corresponding to the final failure of specimen D5-1 is shown in Fig. 10, in which the cracks (signal source) are represented by small balls with the radius representing the normalized energy (indicated by the duration of the signal's trigger time) of the signal source [40–42]. Colors indicate the distance of the AE sources from the central axis of the bolt (i.e.,  $Y = Z = 0$  cm) with warmer color for further distance.

**Crack propagation under different loads.** In order to analyze the crack propagation of the specimen D5-1, a total of 5 load points are selected (load points shown in Fig. 5c). Load points,  $a$ ,  $c$  and  $e$  represent the initial load point, peak load point and residual load point, respectively, and point  $d$  represents the post-peak load point

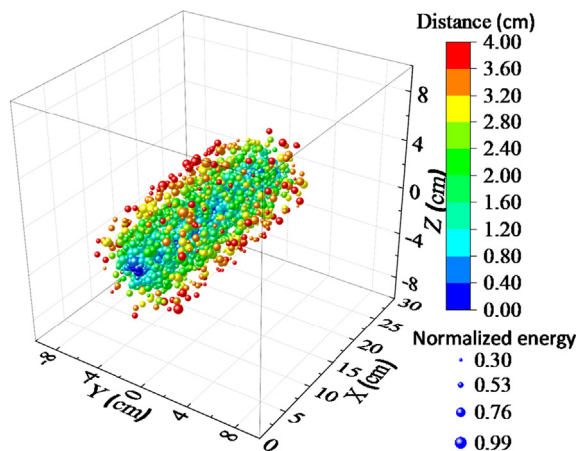


Fig. 10. Distribution of positioning cracks corresponding to the final failure of specimen D5-1 after screening.

adjacent to load point c. The distribution of cracks at all load points are shown in Fig. 11.

The crack gradually expands along the anchoring direction, with bond failure occurring at the bolt-cement mortar interface (Figs. 10 and 11). The debonding length grows with increasing load at a slow (fast) rate before (after) the peak load. With increasing load, the crack expands, which diminishes the cohesion of the bolt interface, weakens the strength of cement mortar, and shortens the effective anchoring length. Once the anchoring force provided by the effective anchoring length no longer balances the tension of the bolt body, an integral decoupling and debonding of the bolt from rock occurs. In addition, the initial crack of specimen D5-1 was close to the model boundary ( $X = 0$  cm), and in the post-peak stage, the crack distribution was relatively uniform along the anchor section. The following is a detailed analysis of the crack growth of specimen D5-1 under different load levels.

The initial crack occurred when the load was about 32.74 kN at the junction of the exposed section of the bolt and the cement mortar material (see Fig. 11a). Tensile deformation emerges as the bolt section was subjected to the load, which led to local relative displacement between the bolt and the surrounding rock and caused the shear failure to firstly occur in this part.

With increasing pull-out load, the local relative displacement between the bolt and surrounding rock gradually increased, which in turn led to the expansion of the debonding length. In addition, the number of cracks decreased from the boundary to the inside of the specimen, as shown in Fig. 11a–c.

Under peak load (see Fig. 11c), cracks penetrated along the bolt body with relatively uniform distribution. A large number of cracks were at the end of the bolt, indicating that the bolt had moved as a whole.

In the afterward stage of the peak load, the failure rate of the anchorage structure increased. Under the action of small loading displacements, the axial load of the bolt decreased rapidly (see Fig. 5c). The entire anchorage section and the rock mass were split apart, which further destroyed the surrounding rock under the shearing effect of the bolt ribs, as indicated by the large debonding length in Fig. 11d.

When the specimen was loaded at point e, the displacement of the bolt was more than 10 mm, which is the distance of the rib spacing. The cracks have been evenly distributed along the bolt (see Fig. 11e). In the subsequent loading process, the number of cracks increased from 3710 to 4434, but the crack distribution pattern stays similar, as shown in Fig. 10.

#### 4. Simulation study of the bolt pulling failure process

Particle flow code (PFC<sup>2D</sup>) can effectively simulate the failure of geotechnical materials and the corresponding crack propagation process [43,44], and is widely applied in solving geotechnical problems [13]. It was used in this part to simulate the pulling failure process of rock bolt.

According to the Section 3.3.2, the failure process of specimens under different curing times has small difference. To conduct a more detailed analysis of the pulling failure process in a limited

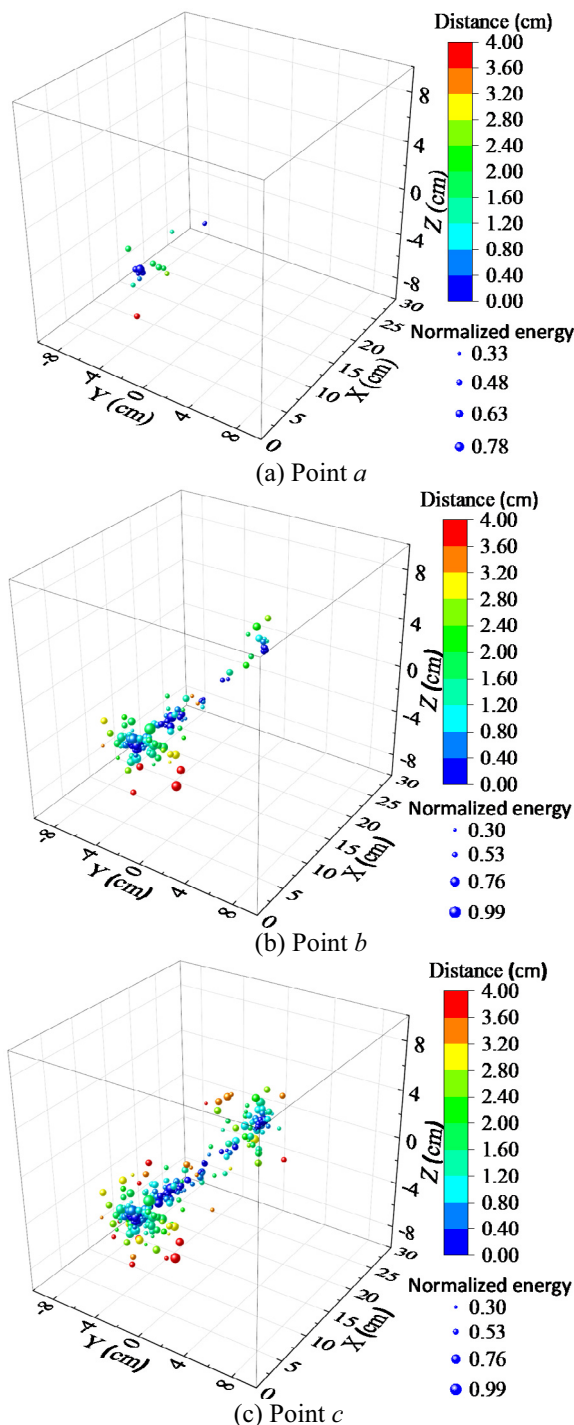


Fig. 11. Crack propagation process of specimen D5-1 under different load levels.

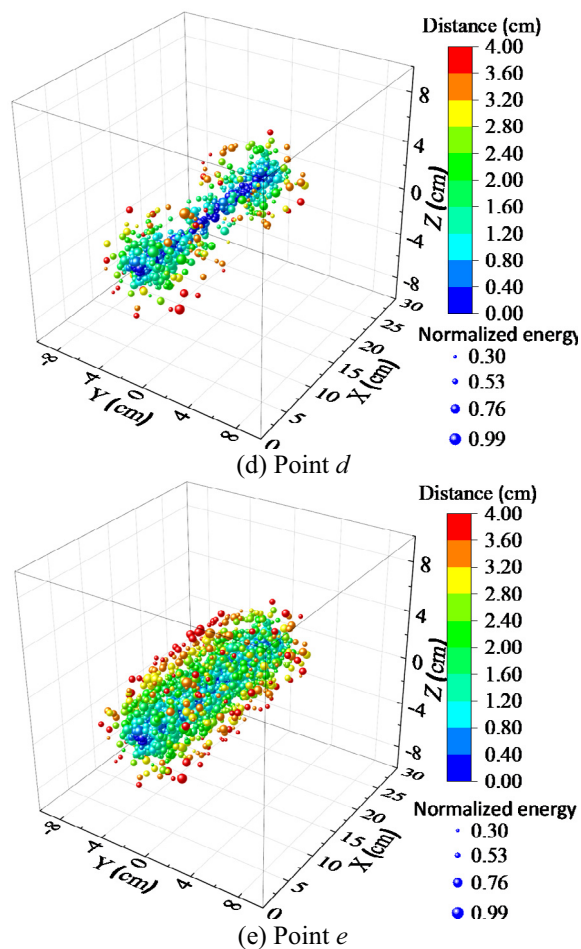


Fig. 11 (continued)

layout, the model corresponding to the specimens D5-1 and D5-2 was analyzed below.

#### 4.1. Particle bonding model

PFC<sup>2D</sup> characterizes geotechnical media as particles with bonds in between. The disk particle in PFC<sup>2D</sup> of unit thickness is rigid with normal and tangential stiffness [48–50]; the bonds suitable for the simulation of geotechnical materials mainly includes the contact bond and the parallel bond (see Fig. 12). Contact bond can reflect the normal and tangential action, but it cannot reflect the moment between particles (see Fig. 12a). Parallel bond can be viewed as a set of springs distributed in a rectangular area centered on the contact point (see Fig. 12b), which transmits both the force and the moment. The contact bond and parallel bond can characterize all the interactions between the particles inside the samples, including the tension, compression, shear, moment and their combined effects. The bonded-particle model (BPM) containing above two bonds was thus used in this study.

#### 4.2. Establishment of calculation model

The numerical model with specimen of actual size and loading method of the testing machine was established using Fish program, as shown in Fig. 13. The synthetic cement mortar material created in PFC<sup>2D</sup> is consistent with that of the actual test sample.

The cement mortar was divided into two groups, i.e. the cement mortar group 1 (particle radius ranges from 0.4 to 0.7 mm) within 5 cm from the bolt axial and the cement mortar group 2 (particle radius ranges from 0.8 to 2 mm) within 5 cm away from the bolt axial, as shown in Fig. 13. For the rock bolt, the exposed length was shortened to 8 cm to simplify the model. The bolt rib spacing and width were set as 10 and 2 mm, respectively.

At the exposed end of the rock bolt, walls were used to apply displacement constraints (see the constraint wall Fig. 13); the loading control method and rate are consistent with that of the experiment (see the loading wall in Fig. 13).

#### 4.3. Determination of simulation parameters

The model's parameters were calibrated by reproducing the load–displacement curves of the actual specimens. In this process, the “trial and error method” [48,51–53] was used to adjust the micro-parameters. The simulated curves were consistent with the experimental results (see Fig. 14). The microscopic parameters of the simulated model (see Table 1) are considered to well represent the mechanical properties of the experimental specimen.

#### 4.4. Simulation results and analysis

To analyze the meso-mechanism of the pulling failure process, the crack distribution, the interaction between bolt and cement mortar material as well as the force field under different loads were investigated, as shown in Figs. 15–17. The selected representative load points were marked in Fig. 14, where points a, c, and f denote the initiation load, peak load and residual load of the crack, respectively. It should be noted that the simulated initial crack dimension is different from the actual crack. This is because that the crack inside the PFC<sup>2D</sup> model, as segment element only representing the breakage of the bond between two adjacent particles, is much smaller than the real crack in terms of scale. Recent studies defined the initial crack load as the load under which the number of cracks reaches one tenth of that of the peak load [48,54–56]. In Fig. 14, the number of cracks at load point a is 16, which is the closest to one tenth of that (176 cracks) at peak load point c, so the point a is set as the initial crack load. In addition, point b is the load point between the load points a and c, and points d and e are the load points between load points c and f. Note that the loading displacement of the bolt corresponding to load point e is about 10 mm (see Fig. 14).

##### 4.4.1. Analysis of crack propagation during pulling failure

The simulated crack growth of the specimen under different pull-out loads were present in Fig. 15. It can be seen that the crack first occurred at the interface of the exposed section of the bolt and the cement mortar material (see Fig. 15a), which is agreed with the crack location of the AE experiment (as shown in Fig. 11a). As the load increases, the cracks gradually expanded inward along the anchorage direction, as indicated by the red arrow in Fig. 15b.

Under peak load (point c), the crack expanded to roughly one third the anchorage length, and some tensile cracks emerged at the end of the anchorage section (see the ellipse box in Fig. 15c). This indicates that the bolt began to undergo an overall displacement under this load. It can be seen from Fig. 14 that the loading displacement of the bolt under peak load had been over 5 mm, so the tensile deformation of the bolt and the compressive deformation of the cement mortar along the anchoring direction together offset the impact of loading on the bolt-cement mortar contact at the end of the bolt.

In the post-peak load stage, i.e., under load points d, e and f, the cracks rapidly expanded along the interface between the bolt and



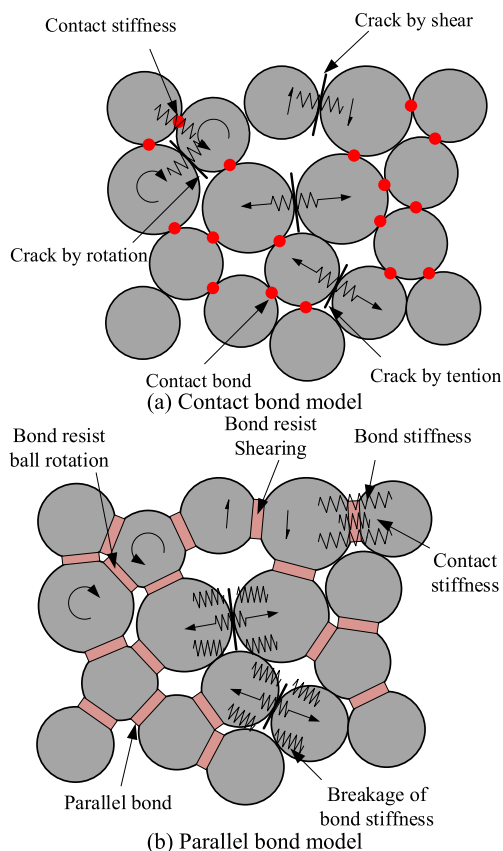


Fig. 12. Cohesive model and its micro-mechanical behavior schematic diagram [45–47].

cement mortar material and penetrated toward the end of the anchorage, as shown in Fig. 15d and e. In particular, the crack under load point e propagated to the end of the anchorage section and connected with the tensile cracks, along with a significant reduction in the anchorage load (see Fig. 14). At this stage, the

overall displacement of the bolt became apparent, and the movement of the bolt left significant space at the end of the anchorage section (see the ellipse box in Fig. 15e).

During the loading process from point e to f, the cement mortar material continued to move to the right under the action of the loading plate, and the space rightward the bolt gradually became larger, as shown in Fig. 15f. Since the overall relative slip between the bolt and the cement mortar material occurred at point e, therefore, the crack distribution did not change significantly during the loading process from point e to f (see Fig. 15f), which is consistent with the results of AE experiment (see Figs. 10 and 11).

#### 4.4.2. Analysis of the interaction between the bolt and cement mortar material

The joint of bolt and cement mortar (denoted by the yellow rectangular box in Fig. 13) was investigated to study the debonding failure process of the bolt. The interaction between the bolt and cement mortar under different loads was shown in Fig. 16. There are 4 bolt ribs contained in the study area; and the cement mortar continuously moves to the right with increasing loading displacement.

Under load point a, the cement mortar left of the bolt rib 1 moved upward due to the dilatancy between the bolt and the cement mortar material (denoted by the red arrows in Fig. 16a). This resulted in the separation of the bolt and cement mortar and the generation of tensile cracks (see the oval box in Fig. 16a). Under load point b, the cement mortar and bolt separated in the entire study area, with a few free particles between the bolt body and cement mortar. Moreover, the upward movement distance of the cement mortar reached the height of the bolt rib (1.4 mm), as shown in Fig. 16b.

When loading to the peak load point c, the bolt ribs moved a certain distance on the cement mortar platforms, as shown in Fig. 16c. The loading displacement reached 5 mm, which is half of the initial bolt rib spacing. However, the location of each bolt rib was not in the center of the corresponding rock platform. This is because the end of the bolt was still attached to the cement mortar. The combined effect of compress deformation of cement mortar and stretch deformation of the bolt led to the relative movement between the bolt rib and rock platform to be less than

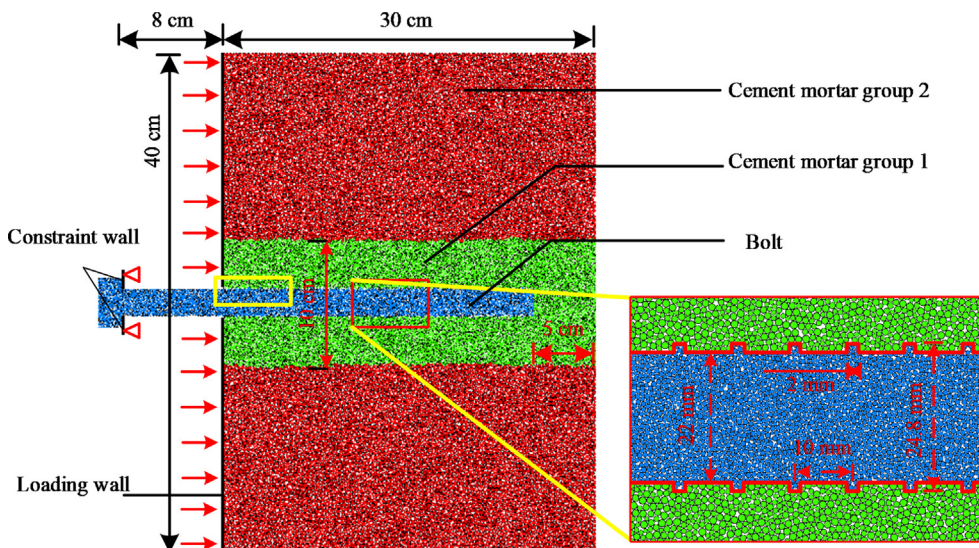


Fig. 13. Calculation model.



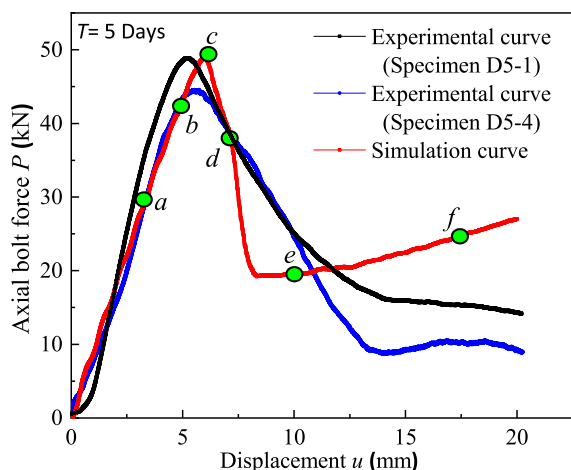


Fig. 14. Comparison of simulation curve and experimental curve ( $T = 5$  days).

Table 1  
Mesoscopic parameters of the numerical model ( $T = 5$  days).

Parameters	Value	
	Cement mortar	Bolt
Density ( $\text{kg}\cdot\text{m}^{-3}$ )	2700	8000
Porosity	0.15	0.10
Contact bond modulus (MPa)	9	100
Contact bond stiffness ratio	0.45	10
Friction coefficient	0.22	1
Parallel bond tensile strength (MPa)	0.45	235
Parallel bond cohesion (MPa)	0.7	170
Parallel bond friction angle ( $^\circ$ )	14	60
Parallel bond modulus (MPa)	9	100
Parallel bond stiffness ratio	0.45	10

5 mm (see the Fig. 15c). Bolt ribs 2 and 3 caused less damage to the platform than that of rib 4 (see the oval box in Fig. 16c). The interaction between the bolt and the cement mortar corresponding to the load point  $d$  is similar to that of the load point  $c$ . In addition, the rib 4 pushes the free particles located left of it to move leftward, as shown by oval box and arrow in Fig. 16d.

When the load displacement reached 10 mm (corresponding to load point  $e$ ), the bolt rib 2, 3 and 4 appeared at roughly the positions (relative to the rock platform) of the original bolt rib 1, 2 and 3, respectively (see the Fig. 16e). This is because the right end of the bolt detached from the cement mortar and an overall displacement of the bolt occurred. Moreover, compared with the load point  $d$ , the axial bolt load at point  $e$  was much lower (see Figs. 14 and 15d).

Under the load point  $f$ , the bolt rib 1 was completely exposed as a result of the movement of the cement mortar (see rib 1 in Fig. 16f). The cement mortar near the bolt has been sheared and broken leading to a large number of free particles between the bolt and the cement mortar, as denoted by the oval box in Fig. 16f.

Overall, it can be seen from Fig. 16 that the dilatancy separation process between the bolt and the cement mortar corresponds to the process of crack propagation, that is to say, the dilatancy effect is the cause of the pulling failure of the bolt during the model load process. Note that tensile micro-cracks are the main failure mode of dilatancy, and only a small number of the shear micro-cracks were generated near the bolt ribs, as shown in Fig. 16.

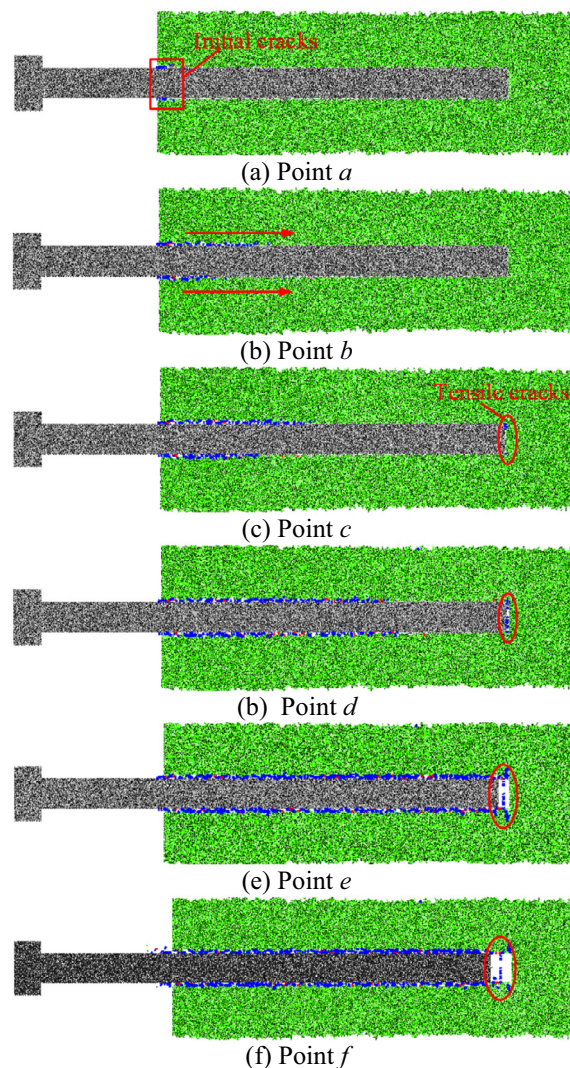


Fig. 15. Crack propagation of specimen under different load levels ( $T = 5$  days) (Blue and red lines respectively represent tensile cracks and shear cracks).

#### 4.4.3. Analysis of force field evolution during pulling failure

The force distribution of the numerical specimen at different load levels is shown in Fig. 17. Warmer color refers to greater force, and the upper limit of the load in Fig. 17 was 4 kN.

For all load levels, the forces between the bolt particles gradually decreased along the left boundary of the cement mortar to the right end of the anchorage section (see the force field in Fig. 17-a-c). Consequently, both the tensile deformation of the bolt and the relative displacement between the bolt and cement mortar gradually decreased rightward along the anchorage [57]. As mentioned in Section 4.4.2, the bolt ribs under load induced the vertical expansion of the cement mortar, resulting in the separation of the cement mortar from the bolt. The separation process can be clearly observed from the the expansion of the rectangular box from Fig. 17a–e. Consequently, the lateral restraining force on the bolt at the dilatation site reduced, and the range of shear force imposed on the the bolt body gradually transferred to the inside of the specimen (denoted by the downward shifting of the red arrows in Fig. 17a–c) until the anchorage body was completely destroyed.

The tensile deformation resulted from the load can lead to the bolt-cement mortar dilatation separation once the load reaches a

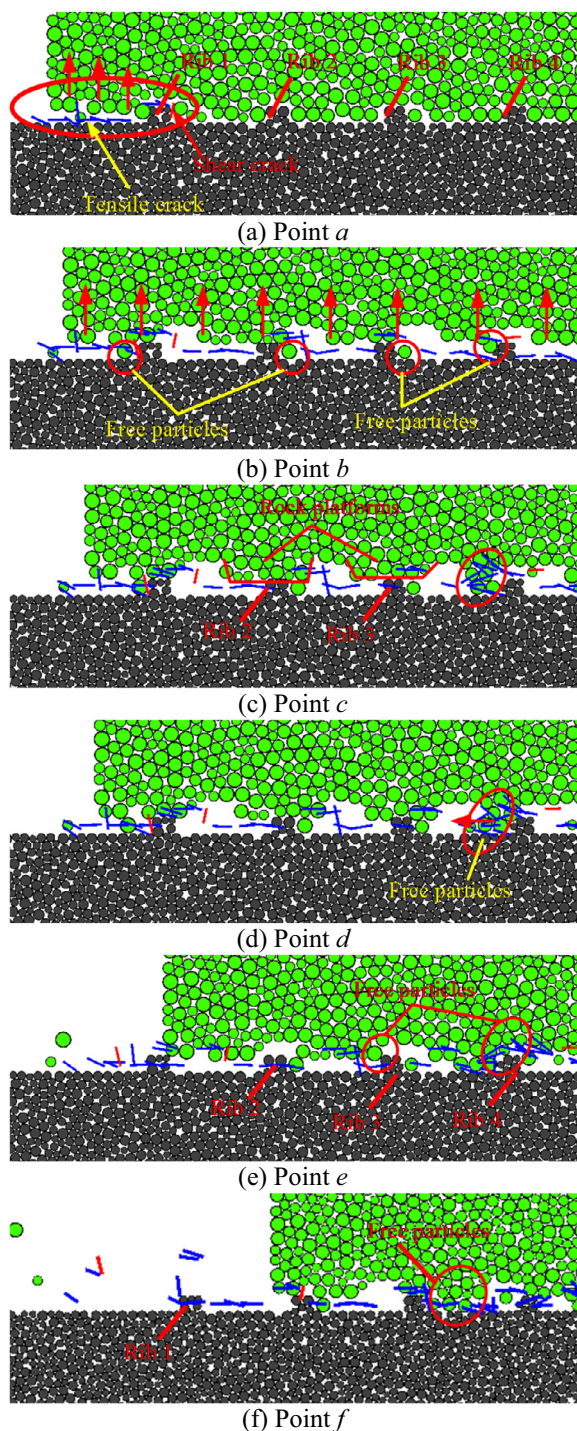


Fig. 16. Interaction between the bolt and cement mortar material ( $T = 5$  days) (Blue and red lines respectively represent tensile cracks and shear cracks).

certain value. As a result, the crack propagation fell behind the transmission of the axial bolt load in the anchorage section, as shown in Fig. 17. This explained the lag observed in Fig. 15, i.e., when the load was applied to point c, the crack spread to one-third of the anchorage section, but the end of the anchorage section of the bolt separated from the cement mortar. It should be pointed out that when the specimen was loaded to the point f, the load on the cross section of the bolt was asymmetrical, with significantly greater load on the lower part of the bolt than that on the upper part, as denoted by the oval box in Fig. 17f.

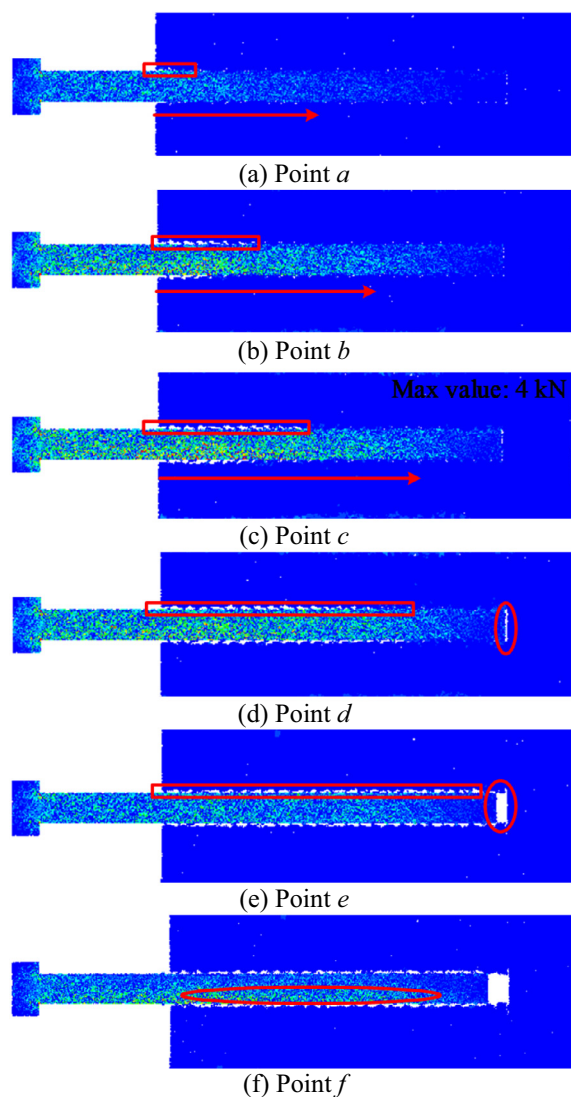


Fig. 17. Force field evolution of the numerical specimen.

### 5. Conclusions

In this study, the bolt-cement mortar meso-interaction in the pull-out failure process was studied with both indoor experiment and PFC<sup>2D</sup> numerical simulation. The cement mortar material was used to pour the bolt pull-out specimens in the experiment. The results are as below:

- (1) Experimental results show that, regardless of the curing time of the specimens, the load displacements of the cement mortar material under peak load were about 5 mm.
- (2) The peak load imposed on the specimen linearly increased with the UCS of the cement mortar.
- (3) The Geiger algorithm based on the LSM is effective in identifying the position of the crack in the experimental specimen. During the loading process, the cracks expand along the anchorage direction, and the debonding length slowly increases before the peak load, but rapidly increases afterward. The failure processes of the specimens under different curing times are similar.
- (4) The PFC<sup>2D</sup> numerical model was calibrated by reproducing the experimental load–displacement curve. Simulation shows that the crack propagation fell behind the axial bolt



load transmission, as under peak load the crack propagated to less than one half of the anchorage length while the tensile crack emerged at the end of the anchorage section.

- (5) The dilatation between the bolt and the cement mortar was identified as the main reason for the pull-out failure of the rock bolt. In the loading process, it caused the cracks and the force field to expand along the anchorage direction.

## Acknowledgments

Financial supports for this work, provided by the National Natural Science Foundation of China (No. 41974164), the Scientific Research Startup Fund for High Level Talents Introduced by Anhui University of Science and Technology (No. 2021yjrc16) and the Chinese Government Scholarship (No. 201906420030), are gratefully acknowledged.

## References

- Shi H, Zhang HQ, Song L, Wu Y. Variation of strata pressure and axial bolt load at a coal mine face under the effect of a fault. *Arch Min Sci* 2019;64(2):351–74.
- Shi H, Zhang HQ, Song L. Evolution of sandstone shear strength parameters and its mesoscopic mechanism. *Geomech Eng* 2020;20(1):29–41.
- Xie S, Pan H, Zeng J, Wang En, Chen D, Zhang T, Peng XJ, Yang JH, Chen F, Qiao SX. A case study on control technology of surrounding rock of a large section chamber under a 1200-m deep goaf in Xingdong coal mine. *China Engineering Failure Analysis* 2019;104:112–25.
- Wu SS, Li JP, Guo JP, Shi GB, Gu QH, Lu CW. Stress corrosion cracking fracture mechanism of cold-drawn high-carbon cable bolts. *Mater Sci Eng, A* 2020;769(2):138479.
- Gao D, Yao W, Wu T. Failure analysis on the axial-connected bolts of the thin-walled cylinder under random vibration loading. *Eng Fail Anal* 2019;105:756–65.
- Wang YJ, Wu ZM, Zheng JJ, Yu RC, Zhou XM. Three-dimensional axisymmetric analytical method for pull-out behaviour of adhesive anchors in concrete. *Eng Fract Mech* 2020;226:106876.
- Teymen A, Kılıç A. Effect of grout strength on the stress distribution (tensile) of fully-grouted rock bolts. *Tunn Undergr Space Technol* 2018;77:280–7.
- Ding Xu, Wu X, Wang Y. Bolt axial stress measurement based on a mode-converted ultrasonic method using an electromagnetic acoustic transducer. *Ultrasonics* 2014;54(3):914–20.
- Torabi AR. On the use of the Equivalent material concept to predict tensile load-bearing capacity of ductile steel bolts containing V-shaped threads. *Eng Fract Mech* 2013;97:136–47.
- Ren FF, Yang ZJ, Chen JF, Chen WW. An analytical analysis of the full-range behaviour of grouted rockbolts based on a tri-linear bond-slip model. *Constr Build Mater* 2010;24(3):361–70.
- Zhang W, Huang L, Juang CH. An analytical model for estimating the force and displacement of fully grouted rock bolts. *Comput Geotech* 2020;117:103222.
- Liu C, Li Y. Predicting the shear resistance contribution of passive fully grouted bolts to jointed rock. *Int J Geomech* 2020;20(2):04019174.
- Yang S, Li M, Song G, Yang Yi, Xie F. Optimization of face flexible bolting and grouting technology for longwall face support under difficult geological conditions. *Energy Sci Eng* 2020;8(4):1260–70.
- Benmokrane B, Chennouf A, Mitri HS. Laboratory evaluation of cement-based grouts and grouted rock anchors. *Int J Rock Mech Min Sci Geomech Abstracts* 1995;32(7):633–42.
- Jasiūnienė E, Mažeika L, Samaitis V, Cicėnas V, Mattsson D. Ultrasonic non-destructive testing of complex titanium/carbon fibre composite joints. *Ultrasonics* 2019;95:13–21.
- Li D, Masoumi H, Saydam S, Hagan PC, Asadzadeh M. Parametric study of fully grouted cable bolts subjected to axial loading. *Can Geotech J* 2019;56(10):1514–25.
- Li Y, Liu Z, Wang Y, Cai L, Zheng M. Experimental study on behavior of time-related preload relaxation for bolted joints subjected to vibration in different directions. *Tribol Int* 2020;142:106005.
- Wu K, Shao Z, Li C, Qin Su. Theoretical investigation to the effect of bolt reinforcement on tunnel viscoelastic behavior. *Arabian J Sci Eng* 2020;45(5):3707–18.
- Liu J, Ouyang H, Feng Z, Cai Z, Liu X, Zhu M. Study on self-loosening of bolted joints excited by dynamic axial load. *Tribol Int* 2017;115:432–51.
- Zhao TB, Guo WY, Yin YC, Tan YL. Bolt pull-out tests of anchorage body under different loading rates. *Shock Vib* 2015;2015:1–8.
- Hyett AJ, Bawden WF, Reichert RD. The effect of rock mass confinement on the bond strength of fully grouted cable bolts. *Int J Rock Mech Min Sci Geomech Abstracts* 1992;29(5):503–24.
- Hu C, Zhou W, Chang XL, Ma G. Study of anchoring of anchor spacing in granular mixture. *Rock Soil. Mech* 2014;35(7):2088–94.
- Jia HS, Pan K, Liu SW, Peng B, Fan K. Evaluation of the mechanical instability of mining roadway overburden: Research and applications. *Energies* 2019;12(22):4265.
- Wu Q, Chen L, Shen B, Dlamini B, Li S, Zhu Y. Experimental investigation on rock bolt performance under the tension load. *Rock Mech Rock Eng* 2019;52(11):4605–18.
- Swissi A, Soussi H, Abid M, Krichen A. Internal and interface shear behaviors of cut and form tapping thread. *Int J Adv Manuf Technol* 2019;105(7–8):3463–75.
- Sun XM, Feng C, Jun Y, Cao WF. Numerical simulation of the effect of coupling support of bolt-mesh-anchor in deep tunnel. *Min Sci Technol* 2009;19(3):352–7.
- Li W, Yang N, Yang B, Ma HY, Li TC, Wang Q, Wang G, Du YT, Zhao MX. An improved numerical simulation approach for arch-bolt supported tunnels with large deformation. *Tunn Undergr Space Technol* 2018;77:1–12.
- Maghous S, Bernaud D, Couto E. Three-dimensional numerical simulation of rock deformation in bolt-supported tunnels: a homogenization approach. *Tunn Undergr Space Technol* 2012;31:68–79.
- Wang JH, Kang HP, Gao FQ. Numerical simulation on load-transfer mechanisms and stress distribution characteristics of cable bolts. *J China Coal Soc* 2008;33(1):1–6.
- Guo W, Xu F. Numerical simulation of overburden and surface movements for Wongwalli strip pillar mining. *Int J Min Sci Technol* 2016;26(1):71–6.
- Wang XQ, Yang JH, Li JZ, Yang L. Analysis of mechanical characteristics of full-length anchor bolts under typical working conditions considering de-anchoring. *J China Coal Soc* 2020;2020:1–10.
- de Buhan P, Bourgeois E, Hassen G. Numerical simulation of bolt-supported tunnels by means of a multiphase model conceived as an improved homogenization procedure. *Int J Numer Anal Meth Geomech* 2008;32(13):1597–615.
- Zhang K, Zhang G, Hou R, Wu Yu, Zhou H. Stress evolution in roadway rock bolts during mining in a fully mechanized longwall face, and an evaluation of rock bolt support design. *Rock Mech Rock Eng* 2015;48(1):333–44.
- Ma CH, Cui KR, Qian JZ, Zha FS. Simulation experiment research on the pulling capacity of pressure bolt. *Chinese J Undergr Space Eng* 2016;12(4):963–7.
- Wu JY, Feng MM, Mao XB, Zhang WL, Ni XY, Han GS. Particle size distribution of aggregate effects on mechanical and structural properties of cemented rockfill: Experiments and modeling. *Constr Build Mater* 2018;193:295–311.
- Shi H, Song L, Chen WL, Zhang HQ, Wang GZ, Yuan GT, Zhang WL, Chen GW, Wang Y, Lin G. New non-destructive method for testing the strength of cement mortar material based on vibration frequency of steel bar: Theory and experiment. *Constr Build Mater* 2020;262:120931.
- Wu JY, Feng MM, Yu BY, Han GS. The length of pre-existing fissures effects on the mechanical properties of cracked red sandstone and strength design in engineering. *Ultrasonics* 2018;82(1):188–99.
- Yang DX, Zhao K, Zeng P, Zhou YL. Numerical simulation of unknown wave velocity acoustic emission localization based on particle swarm optimization algorithm. *Rock Soil Mech* 2019;40(Supp. 1):494–502.
- Geng D, Zhang D, Li Z, Liu D. Feasibility study of ultrasonic elliptical vibration-assisted reaming of carbon fiber reinforced plastics/titanium alloy stacks. *Ultrasonics* 2017;75:80–90.
- Ming P, Lu J, Cai X, Cai X, Liu MY, Chen XD. Analysis of the crack evolution process in crumb rubber concrete based on acoustic emission technology. *KSCE J Civ Eng* 2020;24(7):2088–98.
- Shi GC, Yang XJ, Yu HC, Zhu C. Acoustic emission characteristics of creep fracture evolution in double-fracture fine sandstone under uniaxial compression. *Eng Fract Mech* 2018;210(S1):13–28.
- Wang Y, He M, Ren F, Zhu C, Faramarzi L. Source analysis of acoustic emissions during granite strain burst. *Geomatics Natural Hazards Risk* 2019;10(1):1542–62.
- Guo J, Xu G, Jing H, Kuang T. Fast determination of meso-level mechanical parameters of PFC models. *Int J Min Sci Technol* 2013;23(1):157–62.
- Huang Z, Ma Z, Zhang L, Gong P, Zhang Y, Liu F. A numerical study of macro-mesoscopic mechanical properties of gangue backfill under biaxial compression. *Int J Min Sci Technol* 2016;26(2):309–17.
- Castro-Filgueira U, Alejano LR, Arzúa J, Ivars DM. Sensitivity analysis of the micro-parameters used in a PFC analysis towards the mechanical properties of rocks. *Procedia Eng* 2017;191:488–95.
- Lin H, Oh J, Canbulat I, Stacey TR. Experimental and analytical investigations of the effect of hole size on borehole breakout geometries for estimation of in situ stresses. *Rock Mech Rock Eng* 2020;53(2):781–98.
- Lin H, Kang WH, Oh J, Canbulat I, Hebblewhite B. Numerical simulation on borehole breakout and borehole size effect using discrete element method. *Int J Min Sci Technol* 2020;30(5):623–33.
- Shi H, Song L, Zhang HQ, Xue KK, Yuan GT, Wang ZS, Wang GZ. Numerical study on mechanical and failure properties of sandstone based on the power-law distribution of pre-crack length. *Geomechanics and Engineering* 2019;19(5):421–34.
- Wu J, Jing H, Yin Q, Meng Bo, Han G. Strength and ultrasonic properties of cemented waste rock backfill considering confining pressure, dosage and particle size effects. *Constr Build Mater* 2020;242:118132.
- Wu J, Jing H, Yin Q, Yu L, Meng Bo, Li S. Strength prediction model considering material, ultrasonic and stress of cemented waste rock backfill for recycling gangue. *J Cleaner Prod* 2020;276:123189.
- Shi H, Zhang HQ, Song L, Yang Z, Yuan GT, Xue XR, Wang Y. Failure characteristics of sandstone specimens with randomly distributed pre-cracks under uniaxial compression. *Environ Earth Sci* 2020;79(9).



- [52] Cho N, Martin CD, Segol DC. A clumped particle model for rock. *Int J Rock Mech Min Sci* 2007;44(7):997–1010.
- [53] Chen H, Kimyon O, Lamei Ramandi H, Manefield M, Kaksonen AH, Morris C, et al. Microbiologically influenced corrosion of cable bolts in underground coal mines: The effect of *Acidithiobacillus ferrooxidans*. *Int J Min Sci Technol* 2021;31(3):357–63.
- [54] Yang SQ, Huang YH, Jing HW, Liu XR. Discrete element modeling on fracture coalescence behavior of red sandstone containing two unparallel fissures under uniaxial compression. *Eng Geol* 2014;178:28–48.
- [55] Wang J, Zhang Yu, Qin Z, Song S, Lin P. Analysis method of water inrush for tunnels with damaged water-resisting rock mass based on finite element method-smooth particle hydrodynamics coupling. *Comput Geotech* 2020;126:103725.
- [56] Wang Q, He MC, Li SC, Jiang ZH, Wang Y, Qin Q, Jiang B. Comparative study of model tests on automatically formed roadway and gob-side entry driving in deep coal mines. *Int J Min Sci Technol* 2021;31(4):591–601.
- [57] Sun Y, Li G, Zhang N, Chang Q, Xu J, Zhang J. Development of ensemble learning models to evaluate the strength of coal-grout materials. *Int J Min Sci Technol* 2021;31(2):153–62.